Numerical simulation of flow over a parallel cantilevered flag in the vicinity of a rigid wall

Li Wang[*] and Fang-bao Tian[†]
School of Engineering and Information Technology, University of New South Wales, Canberra ACT, 2600, Australia

(Received 29 December 2018; revised manuscript received 5 March 2019; published 16 May 2019)

Flow over a parallel cantilevered flag in the vicinity of a rigid wall is numerically studied using an immersed boundary–lattice Boltzmann method (IB–LBM) in two-dimensional domain, where the dynamics of the fluid and structure are, respectively, solved by the LBM and a finite-element method (FEM), with a penalty IB to handle the fluid–structure interaction (FSI). Specifically, a benchmark case considering a plate attached to the downstream of a stationary cylinder is first conducted to validate the current solver. Then, the wall effects on the flag are systemically studied, considering the effects of off-wall distance, structure-to-fluid mass ratio, bending rigidity, and Reynolds number. Three flapping modes, including symmetrical flapping, asymmetrical flapping, and chaotic flapping, along with a steady state are observed in the simulations. It is found that the flag is vibrating or stable with a mean angle inclined in the fluid when it is mounted in the vicinity of a rigid wall. The mean inclined angle first increases in the steady state and then decreases in the unsteady state with the off-wall distance. In the unsteady regime, the dependency of the inclined angle on the off-wall distance is similar to that of the gradient of the fluid velocity. In addition, the rigid wall near the flag decreases the lift and drag generation and further stabilizes the flag–fluid system. Contrarily, the flag inertia destabilizes the flag, and large flag inertia induces chaotic vibrating modes.

DOI: 10.1103/PhysRevE.99.053111

I. INTRODUCTION

A flexible plate immersed in a fluid flow is an archetype of fluid–structure interactions, which commonly exists in nature and engineering [1]. In the natural world, biological structures are found to bend, fold, twist, and wave in air and water flows to survive in wavy or windy environment [2]. The understanding of the hidden mechanisms from nature can drive engineering designs [3]. A novel engineering application among them is to harvest energy from flapping flags with built-in piezoelectric materials. The ubiquitous presence of flow makes this renewable energy technique very attractive [4,5]. Another application is fishlike swimming robot, which mimics the locomotion of the fish to swim efficiently [6,7]. These potentials make the study of flapping flags very desirable.

Over the past decades, the flapping flag has been extensively studied. Taneda and Sadatoshi [8] first explored the flapping of flags in a uniform flow experimentally and pointed out that the flag transfers from stable to flapping mode when increasing the inlet velocity. This similar phenomenon was also observed by Zhang *et al.* [1,9] in their gravity-driven soap-film tunnel experiment. They also reported that the flexible filament induces significantly smaller drag compared to the flaglike rigid body. This drag reduction was reproduced in the numerical simulation of a flexible fibre in a two-dimensional moving viscous fluid [10,11]. It is noted that numerical simulations concerning flapping flag becomes popular after the proposal of immersed boundary (IB) method [1,11–14], due to its simplicity and efficiency in handling large structure displacement and deformation. The numerical simulation conducted by Zhu and Peskin using an IB method first pointed out that a certain minimum mass is necessary for the sustained flapping of a flag [12], which is consistent with the theoretical prediction by Shelley *et al.* [15]. Numerical simulation by Tian showed that the nonzero mass is an essential condition for a single flag to establish sustained flapping in the convectively unstable flows, while it is unnecessary for the case of multiflags settled with small separation in the absolutely unstable flows [16]. In the case of multiflags, more flapping modes were observed compared with a single one [12,17–20]. For example, varying the separation distance of three in-line arranged flags, five flapping modes including in-phase mode, symmetric mode, out-of-phase mode, half-frequency mode and irrational-frequency mode were numerically observed [21]. A similar phenomenon in nature is a mother–calf pair of fish. The numerical simulations conducted by Tian *et al.* [7] showed that the coupling of the two fish benefits their swimming performances. Compared with the two-dimensional flag, Huang *et al.* [22] and Tian *et al.* [23] found that the three-dimensional flag is more stable. Huang *et al.* also found that the Strouhal number scales with the density ratio according to $\mathrm{St} \sim \rho_s^{-1/2}$, where ρ_s is the surface density of the flag. In previous studies, most of the flags were immersed in a uniform flow with far-field boundary conditions or symmetrically mounted in a tunnel [11,12,20,21,24,25]. Recently, several studies [26] have been conducted to study the free propulsion performance of a flexible plate in the vicinity of a rigid wall, finding that the ground effects enhance the performance of a self-propelled flexible foil with some

[*]l.wang@unsw.edu.au
[†]f.tian@adfa.edu.au

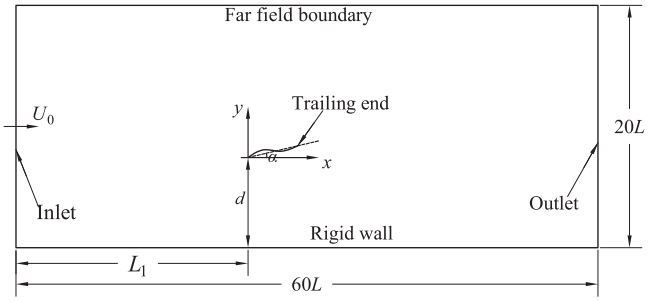

FIG. 1. Schematic of a parallel cantilevered flag in the vicinity of a rigid wall.

specific parameters [27–30], e.g., both Dai *et al.* [31] and Zhang *et al.* [32] pointed out that higher efficiency is obtained when a flexible plate is flapping closer to a wall. However, Blevins and Lauder pointed out that the ground effect does not necessarily enhance the performance of undulating fins [33]. Inspired by the above-mentioned studies, a parallel cantilevered flag in the vicinity of a rigid wall is conducted to study the wall effects on the flapping modes and aerodynamics of the flag. Unlike the foil flapping at a fixed frequency actively, the spontaneous flapping of a flag is fully passive which may present different flapping modes and vortex structures. To the authors' best knowledge, numerical simulation of flow over a parallel cantilevered flag in the vicinity of a rigid wall has not been considered.

In this paper, flow over a parallel cantilevered flag in the vicinity of a rigid wall is numerically studied using an immersed boundary–lattice Boltzmann method (IB–LBM). The arrangements of the rest of this paper are as follows: the physical problem and numerical method are described in Sec. II, with a benchmark case to validate the FSI solver. In Sec. III, the wall effects on the flag are parametrically studied, by considering the effects of off-wall distance, structure-to-fluid mass ratio, bending rigidity and Reynolds number. The influence of the rigid wall on the lift, drag, St number and vibrating amplitude are also systematically discussed. Finally, conclusions of this study are provided in Sec. IV.

II. PHYSICAL PROBLEM AND NUMERICAL METHODS

A. Physical problem

In this work, a parallel cantilevered flag in the vicinity of a rigid wall is considered, as shown in Fig. 1. Due to the presence of wall effects, the flag may flap with a mean angle to the free stream, α, as shown in Fig. 1. Here, α is used to quantify the asymmetrical flapping motion. The fluid is governed by the incompressible viscous Navier-stokes equations. The filament dynamics is governed by the nonlinear Euler–Bernoulli beam equation [16,34,35], i.e.,

$$m_s \frac{\partial^2 \boldsymbol{X}}{\partial t^2} - \frac{\partial}{\partial s}\left[K_s^*\left(\left|\frac{\partial \boldsymbol{X}}{\partial s}\right| - 1\right)\frac{\partial \boldsymbol{X}}{\partial s}\right] + K_b^* \frac{\partial^4 \boldsymbol{X}}{\partial s^4} = \boldsymbol{F}_f, \quad (1)$$

where s is the Lagrangian coordinate along the length, $\boldsymbol{X}$ is the position vector of a point on the filament and $\boldsymbol{F}_f$ is the hydrodynamic stress exerted by the fluid.

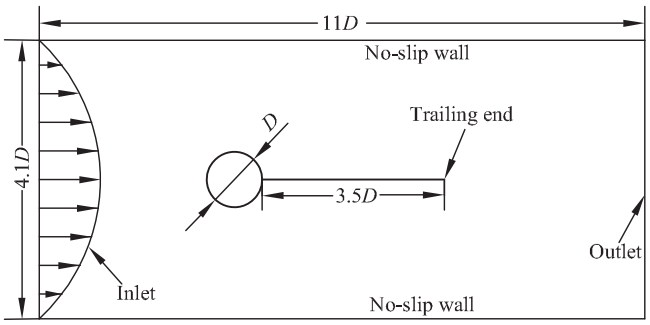

FIG. 2. Schematic of a flexible plate behind a stationary cylinder in a channel.

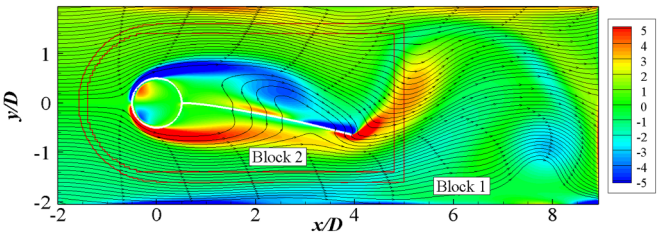

FIG. 3. Instantaneous vorticity contour and stream lines of a flexible plate behind a stationary cylinder in a channel.

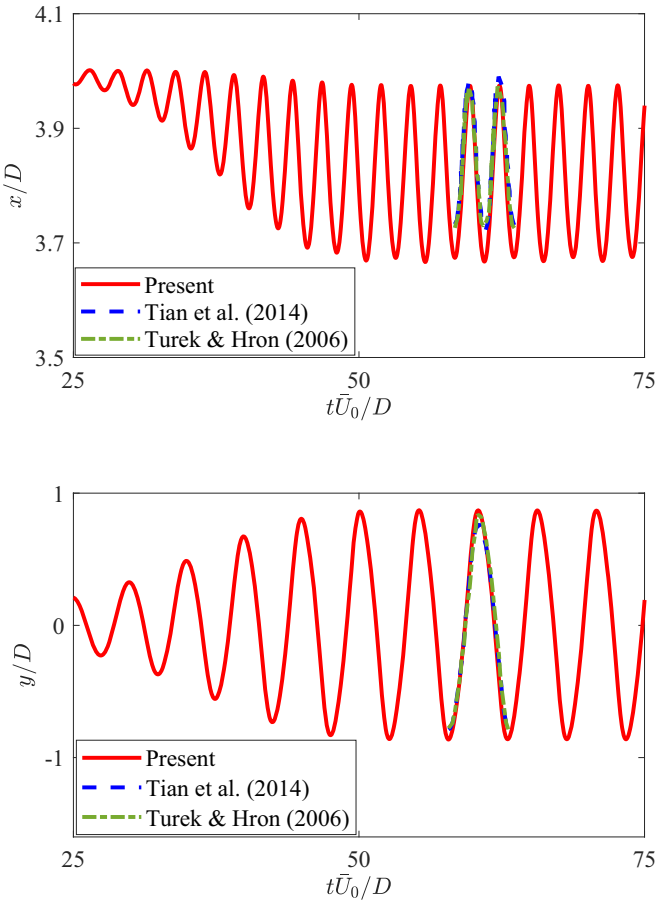

FIG. 4. Comparison of the position histories of the trailing end with the data from Refs. [46,48]: Re = 100, $m^* = 2.0$, and $K_B^* = 1.111$.

TABLE I. Comparison of $C_{D,m}$, St number, and vertical vibrating amplitude of a plate attached behind a stationary cylinder in a channel.

Sources	$C_{D,m}$	St	A_m
Present	4.34	0.19	0.85
Turek and Hron [46]	4.13	0.19	0.83
Tian *et al.* [48]	4.11	0.19	0.78
Bhardwaj and Mittal [47]	3.56	0.19	0.92

Nondimensional parameters governing this problem are

$$\mathrm{Re} = \frac{\rho_f U_0 L}{\nu}, \quad m^* = \frac{m_s}{\rho_f L}, \quad \frac{d}{L},$$
$$K_B^* = \frac{K_B}{\rho_f U_0^2 L^3}, \quad K_S^* = \frac{K_S}{\rho_f U_0^2 L}, \tag{2}$$

where U_0 is the inlet velocity, L is the length of the flag, ν is the viscosity of the fluid, m_s is the linear density of the flag, ρ_f is the density of the fluid, and K_B and K_S are, respectively, the uniform bending rigidity and stretching coefficients along the flag. Unless otherwise stated, $L_1/L = 20$ is used. In this problem, $K_S^* = 500$ is used to achieve a nearly inextensible flag. The drag coefficient, lift coefficient, and Strouhal number are defined as

$$C_D = -\frac{\sum F_x}{0.5\rho U_0^2 L}, \quad C_L = \frac{\sum F_y}{0.5\rho U_0^2 L}, \quad \mathrm{St} = \frac{L}{U_0 T}, \tag{3}$$

where T is the vortex shedding period, and F_x and F_y are, respectively, the horizontal and vertical components of $\boldsymbol{F}_f$ acting on the flag.

B. Numerical methods

The FSI system is solved by using an IB–LBM. In this method, the two-dimensional fluid dynamics is solved by the LBM. A finite-element method is used to solve the structural dynamics, and the complex no-slip boundary conditions on the fluid–structure interface are achieved by an immersed boundary (IB) method. The numerical method used here is briefly reviewed in this section, and the details can be found in Refs. [14,36,37].

In the MRT-based IB-LBM, the evolution equation of the particle distribution function g_i along the ith direction at position $\boldsymbol{x}$ is expressed as [38,39]

$$g_i(\boldsymbol{x} + \boldsymbol{e}_i \Delta t, t + \Delta t) = g_i(\boldsymbol{x}, t) - \Omega_i(\boldsymbol{x}, t) + \Delta t G_i, \tag{4}$$

where $i = 0, 1, ..., 8$, Δt is the time step, $\boldsymbol{e}_i$ is the lattice speed, Ω_i is the collision operator, and G_i represents the body force effects on the distribution function. Ω_i and G_i are defined as

$$\Omega_i = -(M^{-1} S M)_{ij}\left[g_j(\boldsymbol{x}, t) - g_j^{\mathrm{eq}}(\boldsymbol{x}, t)\right], \tag{5}$$

$$G_i = [M^{-1}(I - S/2)M]_{ij} F_j, \tag{6}$$

where M is a 9×9 transform matrix for the two dimensional nine-speed (D2Q9) model, and S is a nonnegative diagonal matrix. The details for the determination of S and M can be found in Ref. [40]. The lattice speed $\boldsymbol{e}_i$ is defined as

$$\boldsymbol{e}_i = \begin{cases} (0, 0), & i = 0, \\ \{\cos[\pi(i-1)/2], \sin[\pi(i-1)/2]\}\frac{\Delta x}{\Delta t}, & i = 1, 2, 3, 4, \\ \sqrt{2}\{\cos[\pi(i-9/2)/2], \sin[\pi(i-9/2)/2]\}\frac{\Delta x}{\Delta t}, & i = 5, 6, 7, 8, \end{cases} \tag{7}$$

where Δx is the lattice spacing. The macro density and momentum are given as follows:

$$\rho = \sum_{i=0}^{8} g_i, \quad \rho \boldsymbol{u} = \sum_{i=0}^{8} g_i \boldsymbol{e}_i + \frac{1}{2}\boldsymbol{f}\Delta t. \tag{8}$$

The local equilibrium distribution function g_i^{eq} and the force term F_i are calculated by

$$g_i^{\mathrm{eq}} = \omega_i \rho \left[1 + \frac{\boldsymbol{e}_i \cdot \boldsymbol{u}}{c_s^2} + \frac{\boldsymbol{u}\boldsymbol{u} : (\boldsymbol{e}_i \boldsymbol{e}_i - c_s^2 \boldsymbol{I})}{c_s^4}\right], \tag{9}$$

$$F_i = \omega_i \left[\frac{\boldsymbol{e}_i - \boldsymbol{u}}{c_s^2} + \frac{\boldsymbol{e}_i \cdot \boldsymbol{u}}{c_s^4}\boldsymbol{e}_i\right] \cdot \boldsymbol{f}, \tag{10}$$

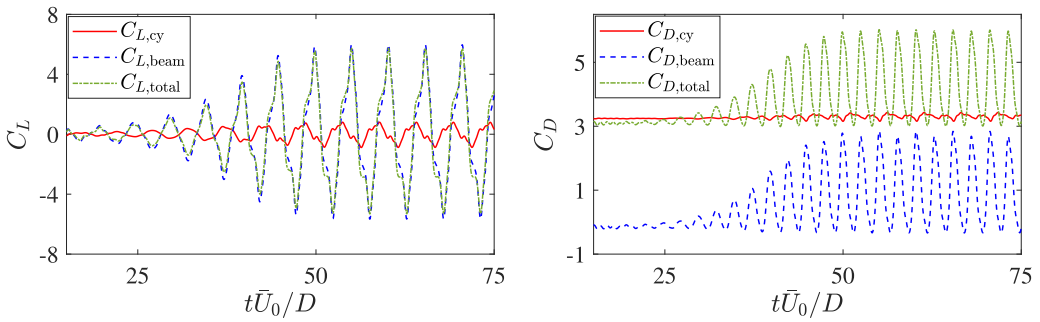

FIG. 5. Time histories C_L and C_D: Re = 100, $m^* = 2.0$, and $K_B^* = 1.111$.

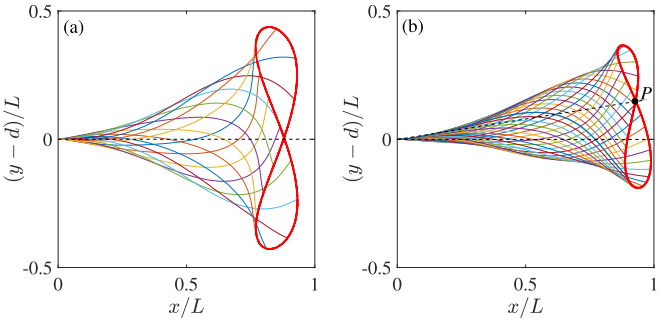

FIG. 6. Flapping patterns of the flag at Re = 100, $m^* = 1.0$, and $K_B^* = 0.0001$: (a) Uniform flow and (b) a rigid wall on the bottom with $d/L = 0.5$.

where the weights ω_i are given by $\omega_0 = 4/9$, $\omega_i = 1/9$ for $i = 1, 2, 3, 4$, and $\omega_i = 1/36$ for $i = 5, 6, 7, 8$. The sound speed $c_s = \Delta x/(\sqrt{3}\Delta t)$, and $\boldsymbol{f}$ is the force acting on the fluid. The relaxation time is related to the kinematic viscosity ν in the Navier–Stokes equations in terms of $\nu = (\tau - 0.5)c_s^2\Delta t$. Nonequilibrium extrapolation method is used for the boundary conditions at the out boundaries of the computational domain [41]. Additionally, the multiblock technique developed by Yu *et al.* [36,37,42] is combined with the geometry-adaptive method to decrease the mesh quantity significantly, and consequently to enhance the computational efficiency.

A finite-element method based on the absolute nodal coordinates formulation (ANCF) is adopted to solve the structural dynamics. The penalty IB method developed by Kim and Peskin [43] is used to handle the no-slip boundaries between the structure and the fluid. The computational domain shown in Fig. 1 extends from left bottom at $(-20L, 0L)$ to right top at $(40L, 20L)$. Extensive preliminary study has been conducted to ensure the domain is large enough to eliminate the boundary effects. Five levels of mesh refinements are used in the present study, with the finest mesh spacing of $D/80$.

C. Validation

The solver used in this work and its early versions have been validated and verified through comparisons with experiments and other numerical studies in unconfined FSI problems [14,16,21,36,44,45]. Here we further validate the solver by considering a plate attached to a stationary cylinder in a channel as shown in Fig. 2. This problem was proposed by Turek and Hron [46] and has been frequently used as a large-displacement benchmark validation for 2D FSI solvers [47,48]. As shown in Fig. 2, a parabolic velocity is applied at the inlet boundary. The average velocity at the inlet $\bar{U}_0$, the diameter of the cylinder D and the fluid density ρ_f are used for nondimensionalization. It should be pointed out that the thickness of the plate is ignored in the current simulation, while it is $0.06L$ (L is the length of the plate) in Refs. [46–48] and does not have a significant effect on the dynamic motion of the plate [49].

In the present simulation, the nondimensional parameters defined in Eq. (2) are Re = 100, $m^* = 2.0$, and $K_B^* = 1.111$. It should be pointed out that the mean velocity is used as the characteristic velocity. A large tension rigidity ($K_S^* = 500$) is used to obtain a nearly inextensible plate. The computational domain extends from left bottom at $(-2D, -2.05D)$ to right top at $(9D, 2.05D)$, and the rigid cylinder is centered at the origin. Two mesh blocks are used to discretize the fluid (see Fig. 3), where the finest mesh spacing (Block 2) around the plate is $D/40$. The Lagrangian mesh spacing of the cylinder and plate is $D/50$.

Figure 4 presents direct comparisons of the position histories of the trailing end of the plate. It is found that the attached plate undergoes a periodic oscillation after $t\bar{U}_0/D = 50$. A comparison of the drag, St number, and vertical vibrating amplitude of the trailing end is presented in Table I. The good agreements with the data from Refs. [46–48] demonstrate the reliability of the current solver. We also note that the time histories of C_L and C_D are not provided in Refs. [46–48]. They are presented in Fig. 5 for future reference.

III. RESULTS AND DISCUSSION

In this study, we will focus on the influence of off-wall distance, structure-to-fluid mass ratio, and bending rigidity. The off-wall distance ranges from $0.1L$ to $2.5L$. Four mass ratios (0.5, 1.0, 2.5, and 5.0) and four bending rigidities ranging from 0.0001 to 0.01 are considered. The Reynolds numbers effects are also examined at Re = 50, 100, 200, and 300. Simulations are conducted until a steady state, a periodic oscillation or a continuous chaotic motion is achieved.

A. Flow regime

Here we first consider the wall effects on the dynamic behaviors of the flag. For comparison, a flag immersed in a uniform flow with far field boundary is also simulated. For a flag in a uniform flow, the flag flaps symmetrically when the far field boundary conditions are applied, as shown in Fig. 6(a). However, the wall effects induce the asymmetrical

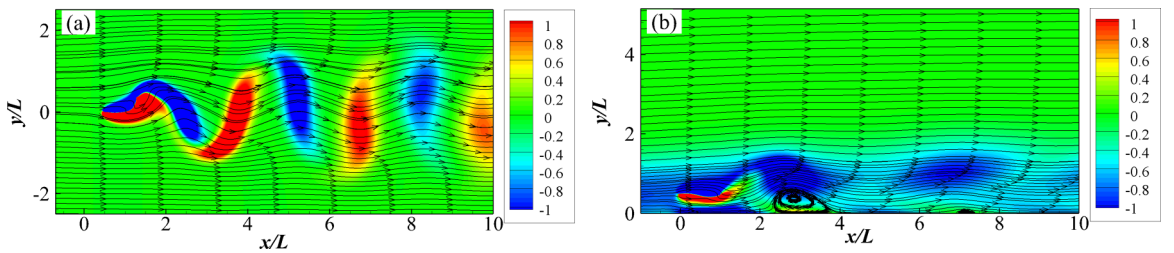

FIG. 7. Instantaneous vorticity contours and stream lines at Re = 100, $m^* = 1.0$: (a) Far field boundary condition and (b) rigid wall on the bottom with $d/L = 0.5$.

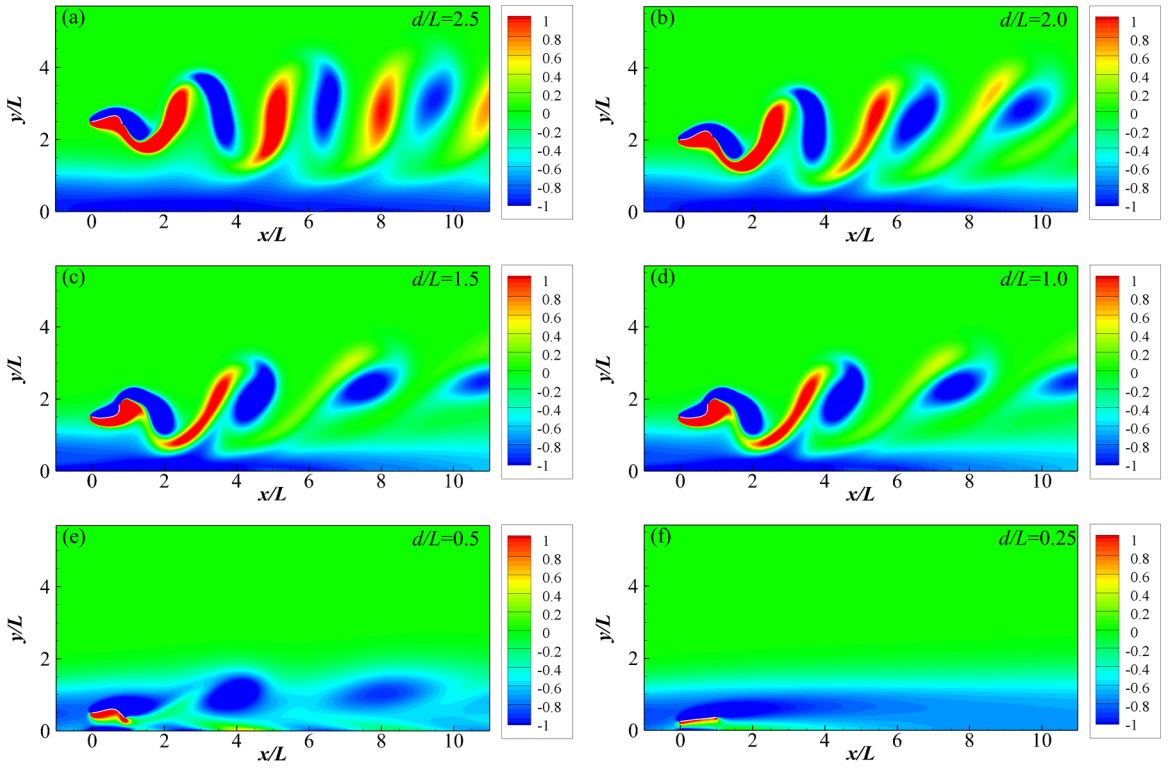

FIG. 8. Instantaneous vorticity contours at Re = 100, $m^* = 1.0$, and $K_B^* = 0.0001$.

flapping motion, as shown in Fig. 6(b). When the flag is mounted in the vicinity of a rigid wall (e.g., $d/L = 0.5$), the trajectory of the trailing end forms an asymmetrical "8," with its equilibrium point [P in Fig. 6(b)] at (0.929, 0.651).

Unlike the symmetrical vortex shedding in the case of uniform flow, only negative vortex is significant when the flag is located in the vicinity of a rigid wall, see Fig. 7. The positive vortex shedding from the trailing end is weakened by the vortices from the rigid wall. The spacing of vortices shown in Fig. 7 also indicates that the wall induces a significantly lower vortex shedding frequency (f). Animations to illustrate the differences of the fluid fields induced by the two flags

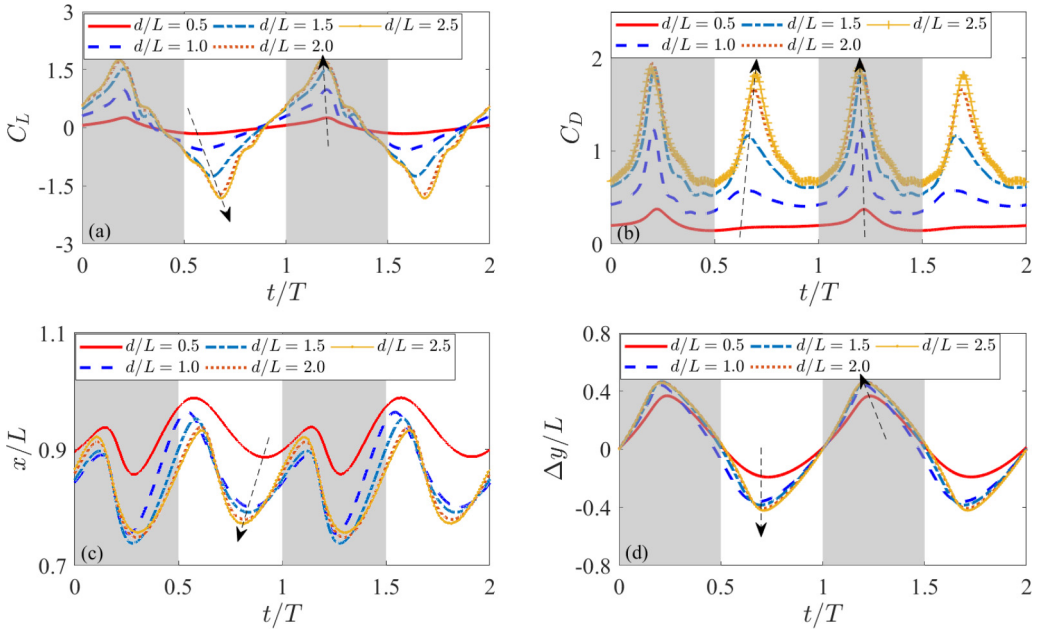

FIG. 9. Comparison of C_L, C_D, x and y positions of the trailing end at Re = 100, $m^* = 1.0$, and $K_B^* = 0.0001$ with d/L ranging from 0.5 to 2.5. Where, the gray and white regions indicate up-flapping and down-flapping, respectively. The arrow denotes the direction that the off-wall distance increases.

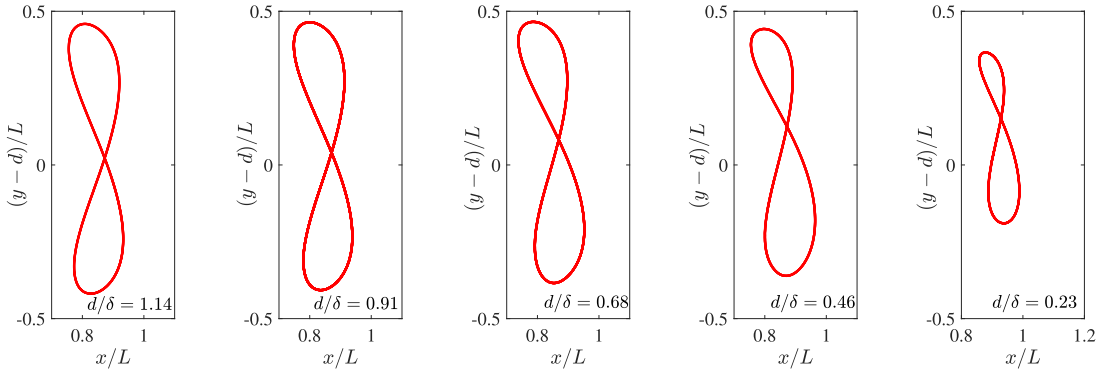

FIG. 10. Trajectories of the trailing ends of flapping flags at Re = 100, $m^* = 1.0$, and $K_B^* = 0.0001$.

are presented as supplements. To study the effects of off-wall distance on the flapping flag, simulations are conducted at Re = 100, $m^* = 1.0$, and $K_B^* = 0.0001$ with d/L ranging from 0.1 to 2.5.

The vortical structures for six typical values of d/L are presented in Fig. 8 from which several observations are obtained. First, the positive vortices shedding from the trailing end of the flag have stronger interaction with the boundary compared to the negative ones. The interaction reduces the strength of the positive vortices, leading to the asymmetrical wake and consequently to asymmetrical flapping of the flag [see Fig. 8 (b)]. Second, the interaction becomes more significant when d/L decreases. If d/L is small enough, e.g., $d/L \leqslant 1.5$, the positive vortices in the near wake of the flag are diminished. Third, when $d/L \leqslant 1.0$, the boundary layer on the rigid wall is destroyed. In addition, only negative vortices are observed in the wake after the vortex interaction as shown in Figs. 8(d) and 8(e). Finally, when d/L reduces to 0.25, a steady state is achieved, as shown in Fig. 8(f). The flag inclines in the fluid without vibration.

Figure 9 presents the time histories of C_D, C_L, x and y coordinates of the trailing end at $d/L = 0.5$, 1.0, 1.5, 2.0, and 2.5. Due to the presence of the vortex rolled-up from the wall boundary, the flag vibrates asymmetrically for the presented cases [see Figs. 9(c) and 9(d)]. Consequently, asymmetrical drag and lift during down-flapping (towards the wall) and up-flapping (leaving the wall) are generated. In addition, Fig. 9(d) shows that the amplitude during up-stroke is comparable with various off-wall distances, while the amplitude during down-flapping is significantly reduced by the rigid wall. It is found that both the lift and drag during up-flapping are larger than those during down-flapping. While, the wall effects on the drag is more significant [see Fig. 9(b)]. The peaks of C_D in the down-flapping phase are almost disappeared at $d/L = 0.5$ and 0.75.

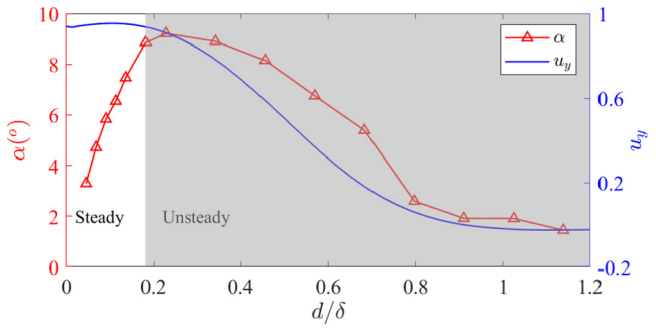

FIG. 11. Mean inclined angles of the trailing ends of flapping flags and the gradient of the horizontal velocity at Re = 100, $m^* = 1.0$, and $K_B^* = 0.0001$.

B. The mean inclined angle

According to the Blasius solution, the boundary layer thickness can be calculated by $\delta = 4.91x/\sqrt{\mathrm{Re}_x}$, where x is the distance downstream from the inlet and $\mathrm{Re}_x = \rho_f u_0 x/\nu$. To normalize the results, the boundary thickness δ is used here to scale the off-wall distance. The trajectories of the flag trailing ends with $d/\delta = 1.14$, 0.91, 0.68, 0.46, and 0.23 are presented in Fig. 10 to illustrate the asymmetrical flapping motion. It shows that the flag is vibrating with a mean angle, as indicated in Fig. 11, to the free stream. In addition, the vibrating amplitude of the flag increases with the off-wall distance and finally is close to that of the flag in a uniform flow. The angle of the equilibrium point defined in Fig. 1 is shown in Fig. 11. When d/δ increases from 0.04 to 1.14, the inclined angle increases if the flag is steady and decreases if the flag is flapping, and its dependency on d/δ in the unsteady regime is similar to that of the gradient of the fluid velocity. When $d/\delta \geqslant 0.9$, the inclined angle is less than 2.0°, the flow around the flag is uniform and the flag is vibrating approximately symmetrically.

To make a clear comparison, the mean drag coefficient ($C_{D,m}$), root-mean-square of lift coefficient ($C_{L,\mathrm{rms}}$), vertical vibrating amplitude (defined as $A_m = A^+ + A^-$, where A^+ and A^- are, respectively, the maximum and minimum vertical displacements of the trailing end), and St number are presented in Fig. 12. It is found that the mean drag, root-mean-square of lift, St number, and vibrating amplitude increase with d/δ. The flag has a lower vibrating frequency when it is mounted closer to the rigid wall. Therefore, the rigid wall stabilizes the vibration of the flag. When $d/\delta \geqslant 0.9$, it is found that the aerodynamic parameters approach to constants. In addition, $C_{D,m}$, $C_{L,\mathrm{rms}}$, and St at $d/\delta = 1.1$ are close those at $d/\delta = 0.9$, with a discrepancy less than 1.0%. Another two series simulations at $L_1/L = 5$ and 10 are also conducted, the results shown in Fig. 12 indicate that d/δ is the key parameter which determines the physics and scales of C_L, C_D, St, and A_m.

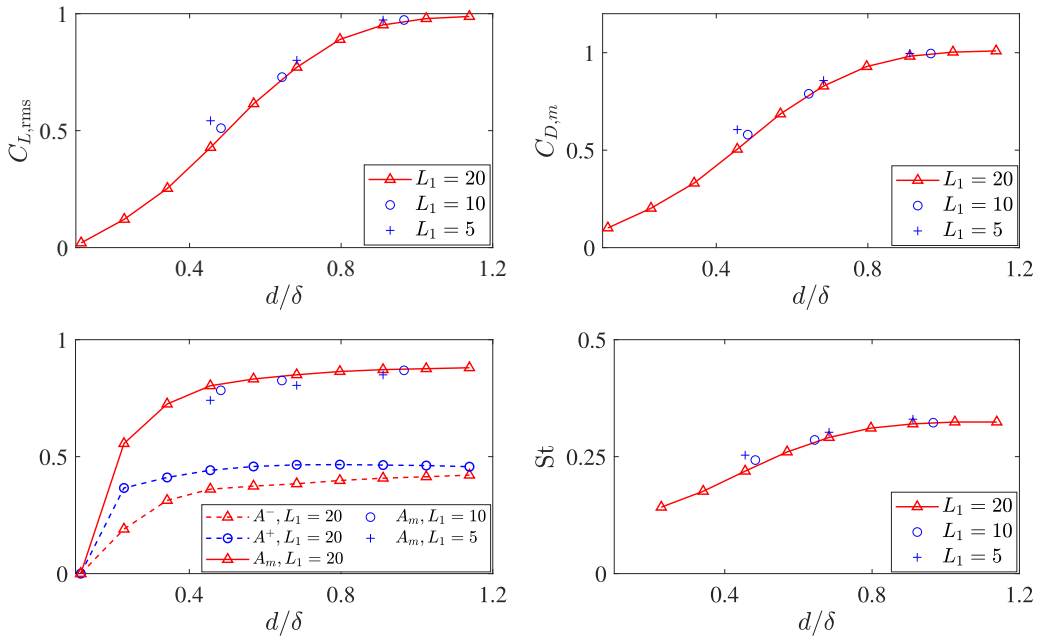

FIG. 12. $C_{L,\mathrm{rms}}$, $C_{D,m}$, vibrating amplitude and St number against off-wall distance at Re = 100, $m^* = 1.0$, and $K_B^* = 0.0001$.

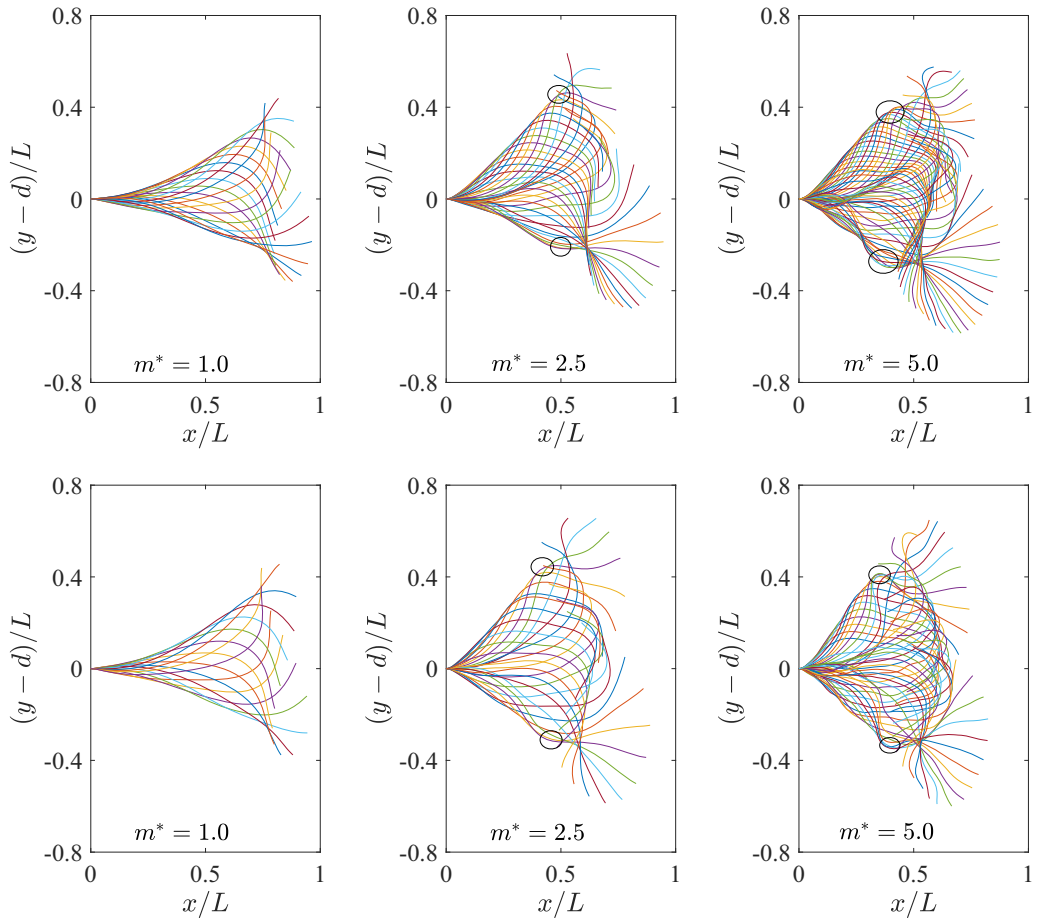

FIG. 13. Flapping patterns of the flag in a period with a nondimensional interval of 0.2: Re = 100, $K_B^* = 0.0001$, $d/\delta = 0.46$ (top) and 0.68 (bottom).

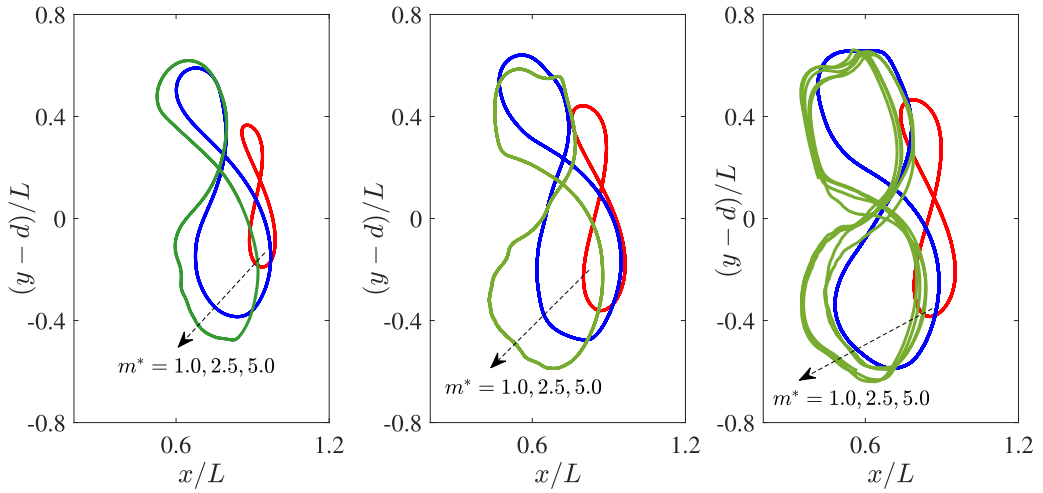

FIG. 14. Trajectories of the trailing ends of flapping flags at Re = 100, $m^* = 1.0$, $K_B^* = 0.0001$, $d/\delta = 0.23$, 0.46, and 0.68 (from left to right).

In conclusion, three modes are observed when a flag is mounted in the vicinity of a rigid wall at Re = 100, $m^* = 1.0$, and $K_B^* = 0.0001$, including symmetrical flapping (at $d/\delta \geqslant 1.1$), asymmetrical flapping ($0.11 < d/\delta < 1.1$) and steady state ($d/\delta = 0.11$). The rigid wall near the flag induces asymmetrical aerodynamic force of the flag. In addition, the wall decreases the lift and drag and correspondingly stabilizes the flag.

C. Effects of structure-to-fluid mass ratio

In this section, three structure-to-fluid mass ratios (1.0, 2.5, and 5.0) are numerically simulated at Re = 100 to study the mass ratio effects. For $m^* = 1$, both fluid and structure inertia are important. For $m^* = 5.0$, the flag inertia is dominant [50].

The flapping patterns of the flag at the three mass ratios at $d/\delta = 0.46$ and 0.68 are presented in Fig. 13. It is found that the flag with higher structure-to-fluid mass ratio deforms more significantly. When $m^* = 1.0$, the deformations of the flag is smooth and periodic. The deformations of the flag at $m^* = 2.5$ and 5.0 have sharp transitions due to the delaying effects of the inertia. In addition, the flapping mode transients from periodic at $m^* = 1$ to chaotic at $m^* = 5$. This transition is consistent with the observations in Refs. [51,52]. These properties are further demonstrated by the trajectories of the trailing ends presented in Fig. 14. It is found that the flapping amplitude increases with the mass ratio. In addition, when the flag is close to the rigid wall ($d/\delta \leqslant 0.46$), all of the three flags obtain periodic asymmetrical flapping. Asymmetrical shape of "8" are obtained for $m^* = 1.0$ and 2.5, but the trajectories

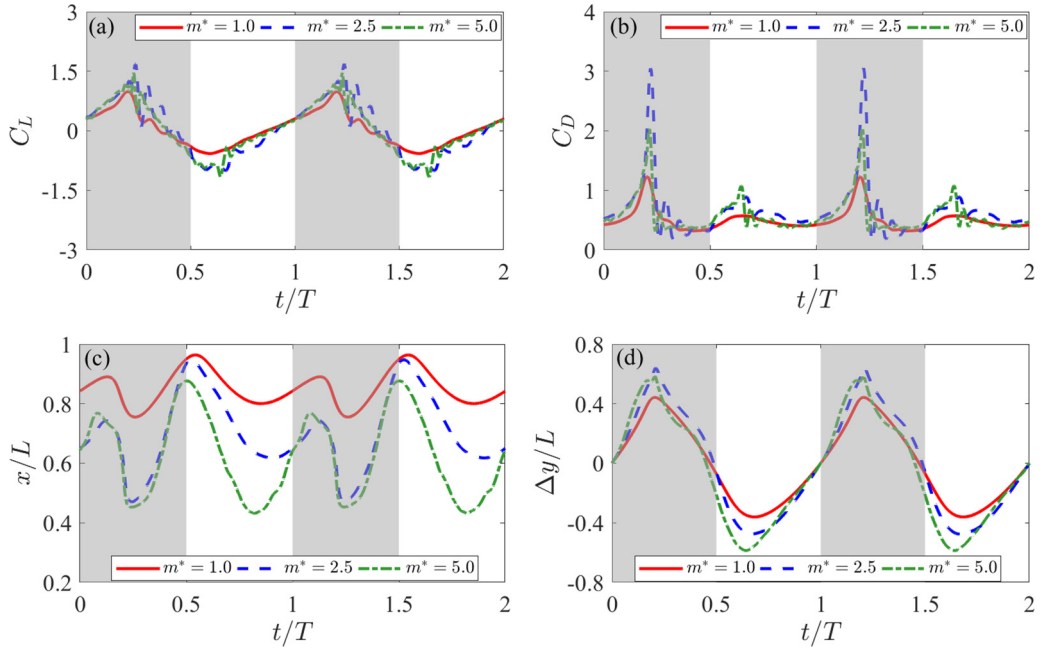

FIG. 15. Comparison of C_L, C_D, x and y positions of the trailing end at Re = 100, $K_B^* = 0.0001$, and $d/\delta = 0.46$. Where, the gray and white regions indicate up-flapping and down-flapping, respectively.

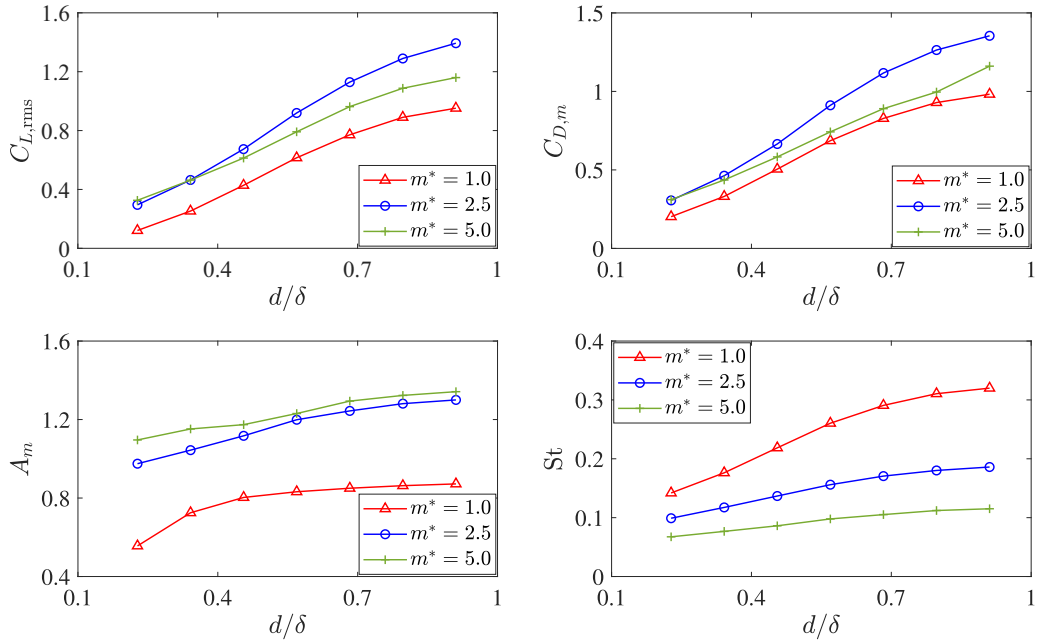

FIG. 16. $C_{L,\mathrm{rms}}$, $C_{D,m}$, A_m, and St number against off-wall distance at Re = 100 and $K_B^* = 0.0001$.

for $m^* = 5.0$ tend to be chaotic. A chaotic flapping mode is observed at $d/\delta = 0.68$ and $m^* = 5.0$ where the flag inertia is dominant.

A direct comparison of the drag, lift, x and y positions at $d/\delta = 0.46$ is shown in Fig. 15. It is found that the lift and drag generated by the flag with larger inertia oscillates more significantly than those with lower inertia, because the deformations of the inertia dominant flag are more significant (see Fig. 13). In addition, the peak values of the drag for the three mass ratios are significantly different, as shown in Fig. 15(b). The peak value of the drag first increases significantly when m^* changes from 1.0 to 2.5, then drops from 3.1 to 2.1 when m^* increases to 5.0. Comparing the time histories of C_D and Δy presented in Fig. 15, it is found that the larger vertical deformation ($|\Delta y|$) induces higher drag peak at $0.2T$ and $0.7T$. It is also noted that the peak drag is more sensitive to the vibrating amplitude of the trailing end in the up-flapping phase than that in the down-flapping phase, which can be reasonably explained by the inclined angle (defined in Fig. 1) of the flag and the low mean flow near the wall.

The mean drag, root-mean square of lift, lift-to-drag ratio, and St number are presented in Fig. 16 for comparison. It is found that the lift, drag, and St number increase with d/δ for all three mass ratios and approach to constants when $d/\delta \geqslant 0.9$. Interestingly, the lift and drag increase when the structure-to-fluid mass ratio raises from 1.0 to 2.5 at each d/δ, but a drop is found at the mass ratio of 5.0. This is demonstrated by the higher peak drags during the up-flapping phase at $0.2T$ induced by the higher peak vibrating amplitude for $m^* = 2.5$. A consistent trend is found for St number at the three mass ratios considered here, i.e., St increases with d/δ, but decreases with the mass ratio. It is also noted that the St number decreases with the mass ratio, which agrees with the results from Ref. [22]. Another series simulations at $m^* = 0.5$ are also conducted to generate the diagram of the dynamic modes of the flag, as shown in Fig. 17. It shows that steady state, asymmetrical flapping, symmetrical flapping and chaotic flapping can be achieved by varying the mass ratio and the off-wall distance. The flag can obtain a steady state more easily at lower mass ratios when decreasing the off-wall distance.

We conclude that the wall effects stabilize the flag at all of the mass ratios considered. Contrarily, the inertia of the flag stimulates the unstable and chaotic flapping modes. It also agrees with the numerical results of a flexible filament attached in the downstream of a rigid cylinder [48]. In addition, chaotic flapping mode is observed when increasing the structure-to-fluid mass ratio.

D. Effects of flag flexibility

Numerical simulations about the highly flexible flag show that the rigid wall stabilizes the flag–fluid system.

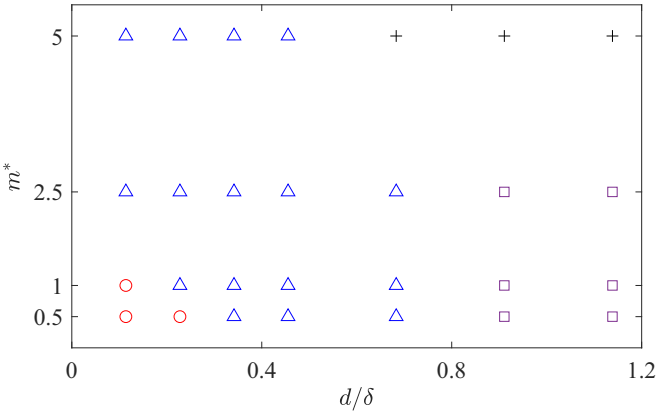

FIG. 17. Dynamic modes of the flag at Re = 100 and $K_B^* = 0.0001$. Where "o," "Δ," "□," and "+" indicate steady state, asymmetrical flapping, symmetrical flapping, and chaotic flapping, respectively.

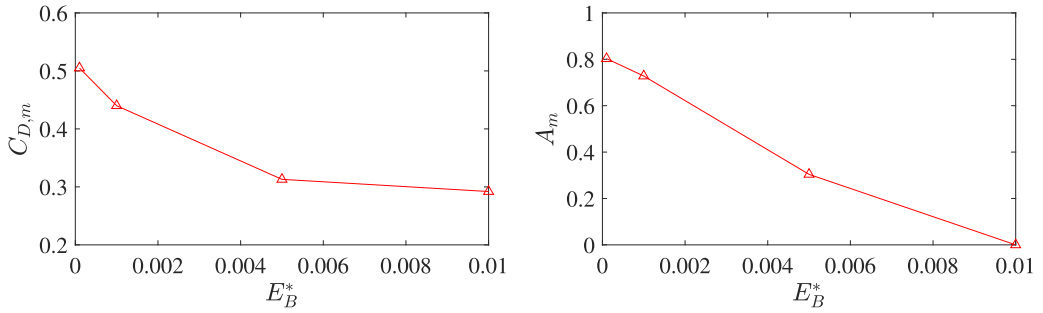

FIG. 18. $C_{D,m}$ and A_m against bending rigidity at Re $= 100$, $m^* = 1.0$, and $d/\delta = 0.46$.

Theoretically, the flag with higher bending rigidity is more stable, as it has a better ability to resist the fluid force. To study the effects of flag flexibility, four nondimensional bending rigidities (0.01, 0.005, 0.001, and 0.0001) are numerically simulated at Re $= 100$, $m^* = 1.0$, and $d/\delta = 0.46$.

The comparison of the mean drag and the vertical amplitude is made in Fig. 18. The results show that the bending rigidity significantly influences the drag and vibrating amplitude, especially when increasing K_B^* from 0.001 to 0.005. But the St number for the flapping flags stays around 0.2 when the bending rigidity is varied. The flag finally obtains a steady state at $K_B^* = 0.01$. The numerical results qualitatively agree with the aforementioned theoretical analysis.

The flapping patterns of the flag flapping in a period are plotted in Fig. 19 for comparison. When the flag is highly flexible ($K_B^* = 0.0001$), a fanlike pattern is observed. With the increase of the bending rigidity, a single neck is formed, and the flapping pattern switches to a single-neck mode. Significant decrease of the flapping amplitude can be directly observed when $K_B^* = 0.005$. The trajectories of the flag trailing end shown in Fig. 20 also indicate that the flag vibrates more symmetrically when increasing the bending rigidity.

E. Effects of Reynolds number

When the flag is mounted close to a rigid wall, the boundary layer decreases the local Reynolds number and brings confinement. Both effects can influence the the aerodynamics of the flag. To study the effects of Reynolds number on the vibrating mode, three additional series simulations for Re $= 50$, 200, and 300 with mass ratio $m^* = 1.0$ and bending rigidity $K_B^* = 0.0001$ are conducted. To decompose the effects of the Reynolds number and the confinement, we introduce the local Reynolds number ($\mathrm{Re}_L = \rho_f u L/\nu$, where u is the local horizontal velocity at the leading edge of the flag, and it is calculated based on the parabolic velocity profile) to rescale the results.

The root-mean-square of lift, mean drag, vibrating amplitude, and St number presented in Fig. 21 show an increase with Re_L. It is noted that even the flag flaps at a same local Reynolds number (e.g., $\mathrm{Re}_L = 100$ and 200), $C_{L,\mathrm{rms}}$, $C_{D,m}$, A_m, and St decrease with the Reynolds number defined in Eq. (2). This indicates that the confinement effects on the aerodynamics of the flag is significant. Take $\mathrm{Re}_L = 100$ as an example, the flapping amplitude of the flag at Re $= 100$ is significantly larger than that at Re $= 200$, because the off-wall distances for Re $= 100$ and 200 are, respectively, $d/\delta = 1.0$ and 0.32. This shows that the confinement of the rigid wall stabilizes the flag. Obviously, the aerodynamics of the flag is then influenced by the dynamic behavior of the flag. As the vibrating amplitude of the flag roughly follows the local Reynolds number Re_L in all the cases considered, a fitting formula using the numerical results are proposed to estimate A_m against Re_L, as shown in Fig. 21.

IV. CONCLUSION

Flow over a parallel cantilevered flag in the vicinity of a rigid wall is numerically studied using an IB–LBM, where the dynamics of the fluid and structure are, respectively, solved by the LBM and a FEM, with a pIB to handle the FSI. A benchmark case considering a plate attached to the downstream of a stationary cylinder is first presented to validate the FSI solver. Then, the wall effects on the flag are systematically studied,

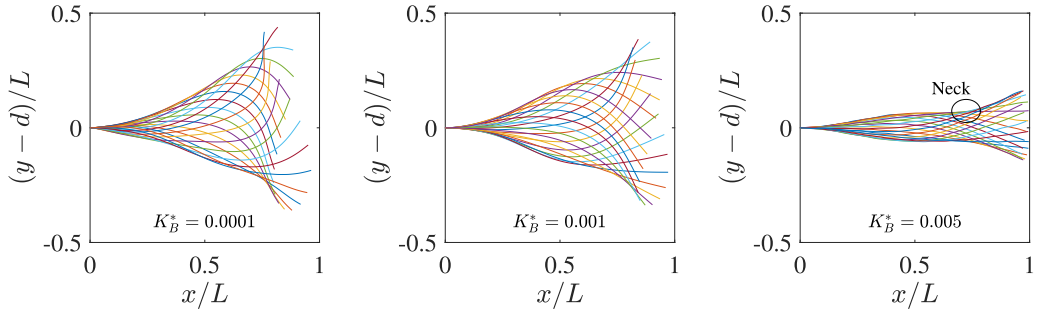

FIG. 19. Flapping patterns of the flag in a period with a nondimensional interval of 0.2: Re $= 100$, $m^* = 1.0$, $d/\delta = 0.46$, $K_B^* = 0.0001$, 0.001, and 0.005.

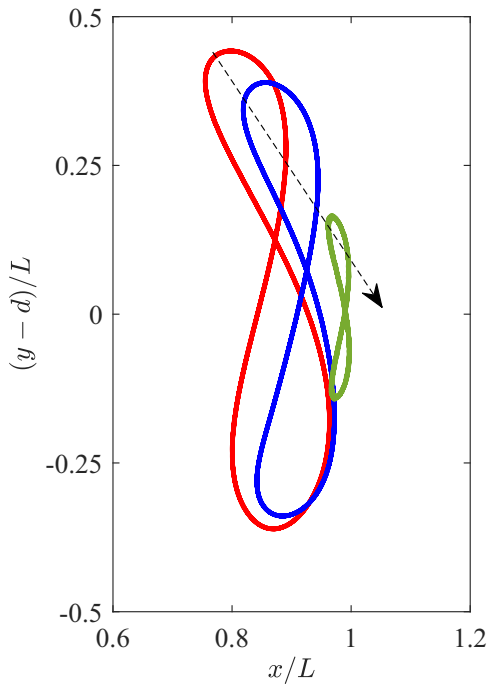

FIG. 20. Trajectories of the trailing ends of flapping flags at Re = 100, $m^* = 1.0$, $d/\delta = 0.46$, $K_B^* = 0.0001$, 0.001, and 0.005. The arrow denotes the direction that the bending rigidity increases.

by considering the effects of off-wall distance, structure-to-fluid mass ratio, bending rigidity and Reynolds number. The interaction of the vortex shedding from the trailing end of the flag and that rolled-up from the wall is analysed. It is found that the flag is vibrating/stable with a mean angle inclined in the fluid when it is mounted in the vicinity of a rigid wall. When d/δ increases from 0.04 to 1.14 at Re = 100 and $m^* = 1.0$, the inclined angle increases if the flag is steady and decreases if the flag is flapping, and its dependency on d/δ in the unsteady regime is similar to that of the gradient of the fluid velocity.

The numerical results show that the rigid wall decreases the lift and drag generation, and further stabilizes the flag–fluid system. Contrarily, the flag inertia destabilizes the flag–fluid system, and large flag inertia induces chaotic vibrating mode, which reduces the lift and drag generation. Numerical results at four different bending rigidities show that the bending rigidity stabilizes the flag–fluid system, and it has a significant influence on the lift, drag, and vibrating amplitude. However, the St number for the flapping flags stays around 0.2 when the bending rigidity is varied.

Parametric studies at four Reynolds number of 50, 100, 200, and 300 show that the lift, drag, flapping amplitude, and St number increase with the off-wall distance and Reynolds number. In addition, the wall effect is decomposed into the confinement effect and the local Reynolds number effect. The results show that the confinement brought by the rigid wall stabilizes the flag.

Among the parameters considered in this work, three flapping modes including symmetrical flapping, asymmetrical flapping, and chaotic flapping, along with a steady state are observed. These modes can be achieved by adjusting the off-wall distance, structure-to-fluid mass ratio, flag bending rigidity, and Reynolds number, which is potentially applicable for the optimization of swimming robots.

ACKNOWLEDGMENTS

Dr. F.-B. Tian is the recipient of an Australian Research Council Discovery Early Career Researcher Award (Project No. DE160101098). This work was conducted with the assistance of resources from the National Computational Infrastructure (NCI), which is supported by the Australian Government.

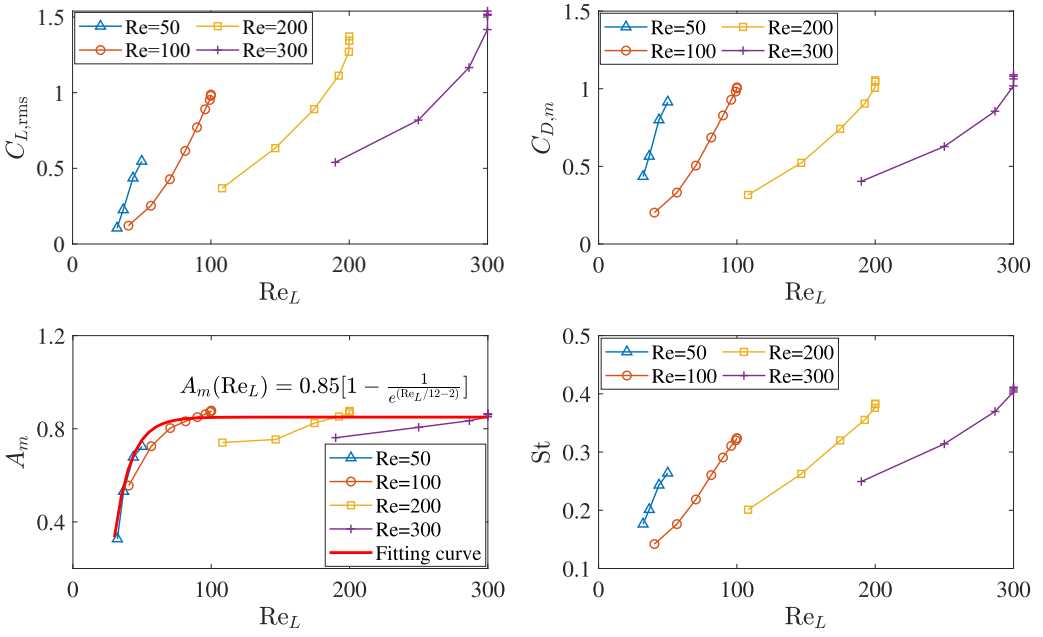

FIG. 21. $C_{L,\mathrm{rms}}$, $C_{D,m}$, A_m, and St number against local Reynolds number at $m^* = 1.0$ and $K_B^* = 0.0001$.

[1] M. J. Shelley and J. Zhang, Flapping and bending bodies interacting with fluid flows, Annu. Rev. Fluid Mech. **43**, 449 (2011).

[2] S. Vogel, *Life in Moving Fluids: The Physical Biology of Flow* (Princeton University Press, Princeton, NJ, 1996).

[3] J. C. Liao, D. N. Beal, G. V. Lauder, and M. S. Triantafyllou, Fish exploiting vortices decrease muscle activity, Science **302**, 1566 (2003).

[4] A. Giacomello and M. Porfiri, Underwater energy harvesting from a heavy flag hosting ionic polymer metal composites, J. Appl. Phys. **109**, 084903 (2011).

[5] D. T. Akcabay and Y. L. Young, Hydroelastic response and energy harvesting potential of flexible piezoelectric beams in viscous flow, Phys. Fluids **24**, 054106 (2012).

[6] H.-B. Deng, Y.-Q. Xu, D.-D. Chen, H. Dai, J. Wu, and F.-B. Tian, On numerical modeling of animal swimming and flight, Comput. Mech. **52**, 1221 (2013).

[7] F.-B. Tian, W. Wang, J. Wu, and Y. Sui, Swimming performance and vorticity structures of a mother–calf pair of fish, Comput. Fluids **124**, 1 (2016).

[8] S. Taneda, Waving motions of flags, J. Phys. Soc. Jpn. **24**, 392 (1968).

[9] J. Zhang, S. Childress, A. Libchaber, and M. Shelley, Flexible filaments in a flowing soap film as a model for one-dimensional flags in a two-dimensional wind, Nature **408**, 835 (2000).

[10] L. Zhu and C. S. Peskin, Simulation of a flapping flexible filament in a flowing soap film by the immersed boundary method, J. Comput. Phys. **179**, 452 (2002).

[11] L. Zhu and C. S. Peskin, Drag of a flexible fiber in a 2D moving viscous fluid, Comput. Fluids **36**, 398 (2007).

[12] L. Zhu and C. S. Peskin, Interaction of two flapping filaments in a flowing soap film, Phys. Fluids **15**, 1954 (2003).

[13] W.-X. Huang, S. J. Shin, and H. J. Sung, Simulation of flexible filaments in a uniform flow by the immersed boundary method, J. Comput. Phys. **226**, 2206 (2007).

[14] F.-B. Tian, H. Luo, L. Zhu, J. C. Liao, and X.-Y. Lu, An efficient immersed boundary-lattice Boltzmann method for the hydrodynamic interaction of elastic filaments, J. Comput. Phys. **230**, 7266 (2011).

[15] M. Shelley, N. Vandenberghe, and J. Zhang, Heavy Flags Undergo Spontaneous Oscillations in Flowing Water, Phys. Rev. Lett. **94**, 094302 (2005).

[16] F.-B. Tian, Role of mass on the stability of flag/flags in uniform flow, Appl. Phys. Lett. **103**, 034101 (2013).

[17] D. Farnell, T. David, and D. Barton, Coupled states of flapping flags, J. Fluids Struct. **19**, 29 (2004).

[18] S. Alben, Wake-mediated synchronization and drafting in coupled flags, J. Fluid Mech. **641**, 489 (2009).

[19] L. Schouveiler and C. Eloy, Coupled flutter of parallel plates, Phys. Fluids **21**, 081703 (2009).

[20] S. Michelin and S. G. Llewellyn Smith, Linear stability analysis of coupled parallel flexible plates in an axial flow, J. Fluids Struct. **25**, 1136 (2009).

[21] F.-B. Tian, H. Luo, L. Zhu, and X.-Y. Lu, Coupling modes of three filaments in side-by-side arrangement, Phys. Fluids **23**, 111903 (2011).

[22] W.-X. Huang and H. J. Sung, Three-dimensional simulation of a flapping flag in a uniform flow, J. Fluid Mech. **653**, 301 (2010).

[23] F. Tian, X. Lu, and H. Luo, Onset of instability of a flag in uniform flow, Theor. Appl. Mech. Lett. **2**, 022005 (2012).

[24] C. Eloy, R. Lagrange, C. Souilliez, and L. Schouveiler, Aeroelastic instability of cantilevered flexible plates in uniform flow, J. Fluid Mech. **611**, 97 (2008).

[25] S. Michelin, S. G. Llewellyn Smith, and B. J. Glover, Vortex shedding model of a flapping flag, J. Fluid Mech. **617**, 1 (2008).

[26] S. Wang, G. He, and X. Zhang, Self-propulsion of flapping bodies in viscous fluids: Recent advances and perspectives, Acta Mechanica Sinica **32**, 980 (2016).

[27] D. B. Quinn, K. W. Moored, P. A. Dewey, and A. J. Smits, Unsteady propulsion near a solid boundary, J. Fluid Mech. **742**, 152 (2014).

[28] D. B. Quinn, G. V. Lauder, and A. J. Smits, Flexible propulsors in ground effect, Bioinspirat. Biomimet. **9**, 036008 (2014).

[29] R. Fernández-Prats, V. Raspa, B. Thiria, F. Huera-Huarte, and R. Godoy-Diana, Large-amplitude undulatory swimming near a wall, Bioinspirat. Biomimet. **10**, 016003 (2015).

[30] S. G. Park, B. Kim, and H. J. Sung, Hydrodynamics of a self-propelled flexible fin near the ground, Phys. Fluids **29**, 051902 (2017).

[31] L. Dai, G. He, and X. Zhang, Self-propelled swimming of a flexible plunging foil near a solid wall, Bioinspirat. Biomimet. **11**, 046005 (2016).

[32] C. Zhang, H. Huang, and X.-Y. Lu, Free locomotion of a flexible plate near the ground, Phys. Fluids **29**, 041903 (2017).

[33] E. Blevins and G. V. Lauder, Swimming near the substrate: A simple robotic model of stingray locomotion, Bioinspirat. Biomimet. **8**, 016005 (2013).

[34] J. Wu, C. Shu, N. Zhao, and F.-B. Tian, Numerical study on the power extraction performance of a flapping foil with a flexible tail, Phys. Fluids **27**, 013602 (2015).

[35] L. Wang, G. M. Currao, F. Han, A. J. Neely, J. Young, and F.-B. Tian, An immersed boundary method for fluid–structure interaction with compressible multiphase flows, J. Comput. Phys. **346**, 131 (2017).

[36] L. Wang and F.-B. Tian, Heat transfer in non-Newtonian flows by a hybrid immersed boundary–lattice Boltzmann and finite difference method, Appl. Sci. **8**, 559 (2018).

[37] L. Xu, F.-B. Tian, J. Young, and J. C. Lai, A novel geometry-adaptive cartesian grid based immersed boundary–lattice Boltzmann method for fluid–structure interactions at moderate and high Reynolds numbers, J. Comput. Phys. **375**, 22 (2018).

[38] X. He and L.-S. Luo, Theory of the lattice Boltzmann method: From the Boltzmann equation to the lattice Boltzmann equation, Phys. Rev. E **56**, 6811 (1997).

[39] Z. Guo and C. Zheng, Analysis of lattice Boltzmann equation for microscale gas flows: Relaxation times, boundary conditions, and the Knudsen layer, Int. J. Comput. Fluid Dyn. **22**, 465 (2008).

[40] Y. Peng, C. Shu, Y.-T. Chew, X. Niu, and X.-Y. Lu, Application of multi-block approach in the immersed boundary–lattice Boltzmann method for viscous fluid flows, J. Comput. Phys. **218**, 460 (2006).

[41] Z. Guo, C. Zheng, and B. Shi, Non-equilibrium extrapolation method for velocity and pressure boundary conditions in the lattice Boltzmann method, Chin. Phys. **11**, 366 (2002).

[42] D. Yu, R. Mei, and W. Shyy, A multi-block lattice Boltzmann method for viscous fluid flows, Int. J. Numer. Methods Fluids **39**, 99 (2002).

[43] Y. Kim and C. S. Peskin, Penalty immersed boundary method for an elastic boundary with mass, Phys. Fluids **19**, 053103 (2007).

[44] Z. Liu, F.-B. Tian, J. Young, and J. C. Lai, Flapping foil power generator performance enhanced with a spring-connected tail, Phys. Fluids **29**, 123601 (2017).

[45] Y.-Q. Xu, Y.-Q. Jiang, J. Wu, Y. Sui, and F.-B. Tian, Benchmark numerical solutions for two-dimensional fluid–structure interaction involving large displacements with the deforming-spatial-domain/stabilized space–time and immersed boundary–lattice Boltzmann methods, Proc. Inst. Mech. Eng., Part C **232**, 2500 (2018).

[46] S. Turek and J. Hron, Proposal for numerical benchmarking of fluid-structure interaction between an elastic object and laminar incompressible flow, in *Fluid-Structure Interaction* (Springer, Berlin, Heidelberg, 2006), pp. 371–385.

[47] R. Bhardwaj and R. Mittal, Benchmarking a coupled immersed-boundary-finite-element solver for large-scale flow-induced deformation, AIAA J. **50**, 1638 (2012).

[48] F.-B. Tian, H. Dai, H. Luo, J. F. Doyle, and B. Rousseau, Fluid–structure interaction involving large deformations: 3D simulations and applications to biological systems, J. Comput. Phys. **258**, 451 (2014).

[49] W. Dettmer and D. Perić, A computational framework for fluid–structure interaction: Finite-element formulation and applications, Comput. Methods Appl. Mech. Eng. **195**, 5754 (2006).

[50] B. Yin and H. Luo, Hydrodynamic interaction of oblique sheets in tandem arrangement, Phys. Fluids **25**, 011902 (2013).

[51] B. S. Connell and D. K. Yue, Flapping dynamics of a flag in a uniform stream, J. Fluid Mech. **581**, 33 (2007).

[52] S. Alben and M. J. Shelley, Flapping States of a Flag in an Inviscid Fluid: Bistability and the Transition to Chaos, Phys. Rev. Lett. **100**, 074301 (2008).